Structure–Property Relationship of Perylene Bisimide Macrocycles Probed by Atomic Force Microscopy and Single-Molecule Fluorescence Spectroscopy

Ji-Eun Lee,[†] Vladimir Stepanenko,[‡] Jaesung Yang,[†] Hyejin Yoo,[†] Felix Schlosser,[‡] Daniel Bellinger,[∥] Bernd Engels,[∥,*] Ivan G. Scheblykin,[§,*] Frank Würthner,[‡,*] and Dongho Kim[†,*]

[†]Spectroscopy Laboratory for Functional π-Electronic Systems and Department of Chemistry, Yonsei University, Seoul, 120-749, Korea, [‡]Institut für Organische Chemie and Center for Nanosystems Chemistry, Universität Würzburg, 97074, Würzburg, Germany, [§]Chemical Physics, Lund University, Box 124, 22100, Lund, Sweden, and [∥]Institut für Physikalische und Theoretische Chemie, Universität Würzburg, 97074 Würzburg, Germany

ABSTRACT Properties of a series of acetylene-linked perylene bisimide (PBI) macrocycles with different ring size composed of three to six PBI dyes were investigated by atomic force microscopy (AFM) and single-molecule fluorescence spectroscopy in a condensed phase. It was demonstrated that the structures of PBI cyclic arrays (*CN*s, $N = 3$, 4, 5, and 6) become distorted with increasing the ring size through molecular dynamics (MD) simulations (PM6-DH2 method) and AFM height images of *CN*s on highly ordered pyrolytic graphite (HOPG) surface. The MD simulations showed that only C5 and C6 rings are highly flexible molecules whose planarization goes along with a significant energetic penalty. Accordingly, both molecules did not show ordered adlayers on a HOPG surface. In contrast, C3 and C4 are far more rigid molecules leading to well-ordered hexagonal (C3) and rectangular (C4) 2D lattices. At the single-molecule level, we showed that the fluorescence properties of single *CN*s are affected by the structural changes. The fluorescence lifetimes of *CN*s became shorter and their distributions became broader due to the structural distortions with increasing the ring size. Furthermore, the *CN*s of smaller ring size exhibit a higher photostability and an efficient excitation energy transfer (EET) due to the more well-defined and planar structures compared to the larger *CN*s. Consequently, these observations provide evidence that not only PBI macrocycles are promising candidates for artificial light-harvesting systems, but also the photophysical properties of *CN*s are strongly related to the structural rigidity of *CN*s.

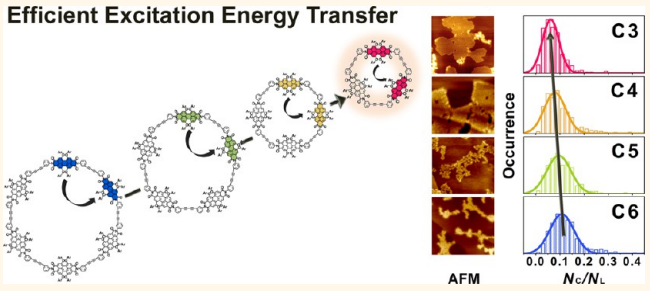

KEYWORDS: macrocycles · light-harvesting system · excitation energy transfer · atomic force microscopy · single-molecule spectroscopy · molecular dynamics simulations

One of the most fascinating objectives in materials, physical, and chemical sciences is the invention of large macrocyclic architectures with well-defined circular geometry, similar to that of natural light-harvesting (LH) complexes, in order to collect light and transfer its energy in space for the sake of applications in organic electronics. To mimic the attractive features of fertile LH and efficient excitation energy transfer (EET) processes of the natural LH complexes,[1,2] various macrocyclic pigment arrays have been envisaged and synthesized.[3−8] Especially, the synthesis of acetylene-based macrocycles has successfully been utilized for preparing the rigid macrocyclic scaffolds by connecting the constituent chromophores.[9−12]

Perylene bisimide (PBI) molecule has been well recognized as a versatile chromophore with strong absorption, near unity fluorescence quantum yield, and high photostability.[13,14] Owing to these appealing properties, PBI derivatives have been utilized in various electronic and optical applications such as field-effect transistors[15,16] and optoelectronic/photonic devices such as photoconductors, photovoltaic cells, and

* Address correspondence to dongho@yonsei.ac.kr, wuerthner@chemie.uni-wuerzburg.de, Ivan.Scheblykin@chemphys.lu.se, bernd.engels@mail.uni-wuerzburg.de.

Received for review February 5, 2013 and accepted May 8, 2013.

Published online May 08, 2013
10.1021/nn400616u

Chart 1. Molecular structures of PBI monomer (M1) and PBI cyclic arrays (*CN*s)

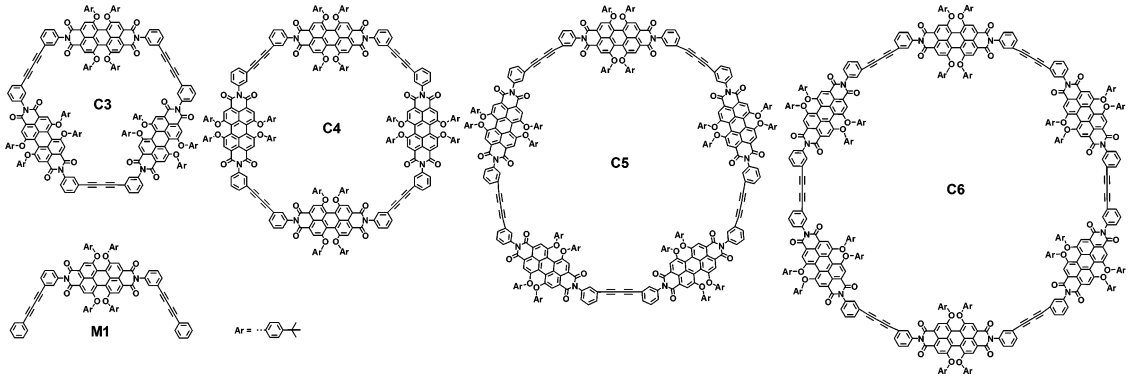

light-emitting diodes.[17−19] As continuous efforts to develop new molecular assemblies based on PBI dyes, a series of acetylene-linked PBI macrocyclic structures have been synthesized most recently with varied ring size containing three to six 1,6,7,12-tetraphenoxy-PBI chromophores (*CN*s, *N* = 3, 4, 5, and 6; Chart 1).[20] Their photophysical properties were studied by time-resolved spectroscopy at the ensemble level,[21] providing valuable information on average properties of the macrocycles. When applied to a complex system, however, it has frequently missed the real complexity of the sample, since different populations within the sample may contribute to the detected signal, possibly giving rise to erroneous interpretation of the data. Also, our understanding of their topologies and how the photophysical properties arise from the interaction between chromophores within the cyclic arrays, is limited. In this regard, it is necessary to perform atomic force microscopy (AFM) and single-molecule spectroscopy (SMS) measurements and to link the results by molecular dynamics (MD) calculations.[22] Toward this goal, PBI dyes are most suitable chromophores for such studies owing to their high fluorescence quantum yields (close to unity) and superb photostability.[23−27]

SMS[28−32] has proven to be a powerful tool to allow observation of dynamic processes in individual molecules *via* monitoring their fluorescence properties as a function of time.[33−42] SMS can also study heterogeneous processes based on distributions of physical quantities such as fluorescence lifetimes,[33,34] since the detection of individual molecules effectively prevents ensemble averaging effect at bulk level, and enables us to detect unprecedented events.

In this study, we have investigated the photophysical properties of *CN*s with a focus on the relationships between the structural rigidity of *CN*s and the EET processes in the solid state. The first part discusses the results of AFM to explore the structural rigidity *via* the image of the self-assembled *CN*s on highly ordered pyrolytic graphite (HOPG) surface. To make sure of the structural information of *CN*s, we compute the optimized geometries of *CN*s and MD simulations using the PM6-DH2 method. On the basis of the structural information, we deal with the fluorescence dynamics of single *CN* molecules in relation to their structural changes. Photobleaching dynamics, and photostability *via* on-times at the first intensity level in the fluorescence intensity trajectories (FITs), as well as fluorescence lifetimes were measured at the single-molecule level. To reveal the EET processes in the *CN*s, the fluorescence polarization trajectories *via* fluorescence polarization technique at the single-molecule level were measured. Lastly, we show how the structural information of *CN*s has influence on the EET efficiency in *CN*s by performing a coincidence measurement at the single-molecule level.

We highlight that our study is the first attempt not only to examine their topologies by AFM, and the single-molecule fluorescence dynamics of PBI macrocyclic arrays through various single-molecule spectroscopic measurements as top-down and bottom-up experiments, but also to provide further insight into the structure/property relationship to fabricate the artificial LH systems for the practical usage in the solid state.

RESULTS AND DISCUSSION

Atomic Force Microscopy. AFM measurements were performed to investigate the molecular structures and self-assembly behaviors of PBI macrocycles with an increase of the ring size. The samples were prepared by spin-coating a 7.5×10^{-6} M solution onto HOPG surfaces. Figures 1−3 and Figures S1−S5 (see Supporting Information) show the AFM height images of the respective *CN*s that are composed of three up to six PBI subunits and PBI monomer (**M1**). The degree of order of the observed domains as well as the unit cells is very different for various *CN*s and clearly dependent on the ring size. Especially, the self-assembled monolayer with a highly ordered hexagonal nanopattern consisting of a donut-like structure was observed for **C3** spin-coated from a methyl-cyclohexane (MCH)/tetrahydrofurane (THF) (93:7 vol %) solution onto HOPG (Figure 1a,b).[20] The distances determined from the AFM images support the proposed arrangement of six individual **C3** forming a hexagonal structure that resembles a donut.

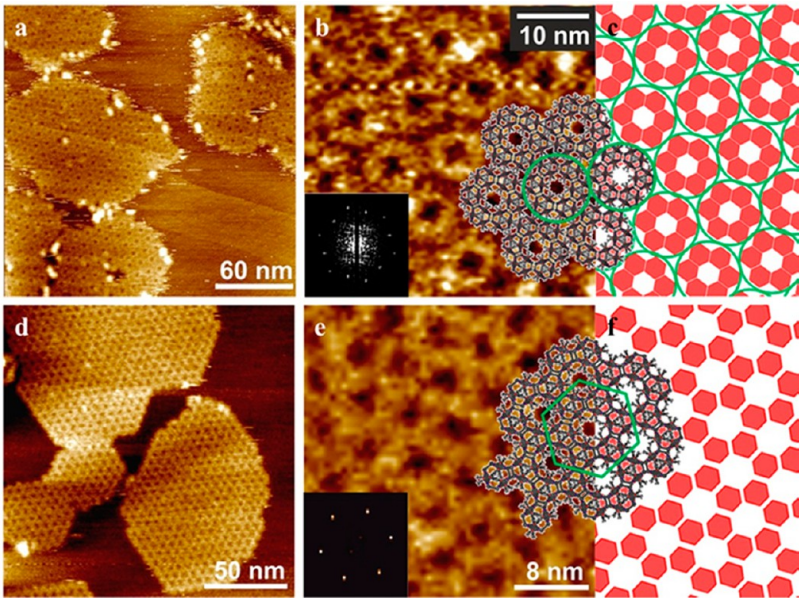

Figure 1. AFM height images of C3. (a,b) Monolayer of C3 arranged in a donut-like structure which was obtained by spin-coating from MCH/THF (93:7 vol %) solution. (c) Schematic presentation of the donut-like pattern; the red hexagons resemble the C3. (d,e) Monolayer of C3 arranged in a honeycomb-like structure obtained by spin-coating from THF solution. The AFM images in panels b and e are partly overlaid by the proposed models; insets in panels b and e show the respective 2D FFT graph. (f) Schematic presentation of the honeycomb-like pattern; the red hexagons resemble the C3.

The modeled structures that overlay the AFM image are shown in Figure 1b. In Figure 1c a schematic presentation of the arrangement is shown, where red hexagons resemble the **C3**, and the green circles therein highlight the donut-shaped structures and visualize their hexagonal assembly next to each other. The 2-dimensional Fast Fourier Transform (2D FFT) analysis was performed on images with periodic structure to calculate the unit cell dimensions. The 2D FFT analysis depicts two distinct hexagonal symmetries (3.6 ± 0.2 nm and 4.5 ± 0.2 nm) that are rotated by about 30° with respect to each other (Figure 1b). Furthermore, this analysis indicates additional reflection characteristics of a hexagonally packed system with a frequency of 8.9 ± 0.2 nm corresponding to the distance between donut holes. The width of the donut wall was measured to be 2.5−2.8 nm, which is related to the calculated diameter of **C3**. These findings support the proposed model of six **C3** macrocycles forming donuts, which are arranged in a hexagonal array next to each other. Interestingly, a sample of **C3** spin-coated from a pure THF solution showed a different nanopattern, that is, highly ordered domains, resembling a honeycomb-like structure (Figure 1d,e; additional AFM images are shown in the Supporting Information, Figure S1). The height of this honeycomb structure was estimated from a cross-section analysis (see Figure S1) to be 0.3 ± 0.1 nm and, therefore, indicating a monolayer. The proposed arrangement is illustrated in Figure 1e in the form of a model that superimposes the AFM image. Owing to the limited resolution of the AFM imaging technique, it was not possible to determine the orientation of the molecules in honeycomb pattern.[43−45] The center-to-center distance between the holes in the proposed model is 4.8 nm, which is in a good accordance with the distance (4.6 ± 0.2 nm) determined from the AFM image. Thus six **C3**s constitute a hexagon (marked by a green hexagon in Figure 1e,f; in the latter also a schematic presentation of the arrangement is shown, where red hexagons resemble the **C3**). The hexagons are situated right next to each other and lead to the honeycomb-like pattern on the surface. Shown in the inset in Figure 1e is the FFT of the AFM image showing reflections characteristic of a hexagonally packed system (with a frequency of 4.6 ± 0.2 nm), which is in accordance with the proposed model of a honeycomb arrangement.

The three bulky tetraphenoxy-PBI cores of the macrocycle may be regarded as pillars that determine the interaction with the surface of the HOPG. Both types of monolayers appear to have the same coverage (density has been estimated to be 9−10 molecules per 100 nm^2). We assume that in the case of the honeycomb-like pattern no significant interactions occur between the molecules, which could be oriented either with PBI cores or diacetylene units or even PBI and diacetylene units next to each other. Therefore, this arrangement is defined by the template effect of HOPG and we can even imagine that the three possible intermolecular arrangements form in a random way owing to the nearly hexagonal shape of the molecules. In contrast, the donut-like pattern was probably formed as a result of interactions between the

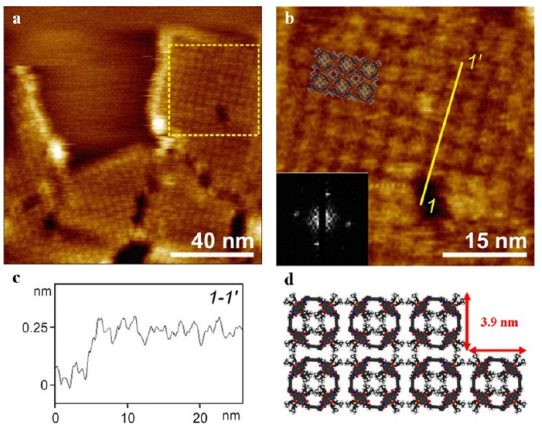

Figure 2. AFM height images of C4. (a,b) Monolayer of C4 obtained by spin-coating from $CHCl_3$ solution onto HOPG; (b) a magnified area in panel a indicated by the yellow dashed square. (c) Cross-section analysis along the yellow line 1−1′ in panel b. (d) Illustration of the proposed model of the self-assembled arrangement. The AFM image in panel b is partly overlaid by this model; inset in panel b shows the 2D FFT graph.

molecules, which are very strong in aliphatic MCH solution, even between PBIs bearing bulky phenoxy substituents.[46−48] Therefore, we suppose that next to the interaction between molecule and HOPG, the strong molecule−molecule interaction plays an important role in the arrangement of the donut-like structure.

The AFM images of **C4** are shown in Figure 2a,b. Highly ordered domains resembling the rectangular structure of **C4** have been observed after spin-coating from $CHCl_3$ solution (for additional AFM images, see Supporting Information, Figure S2). The height was determined from a cross-section analysis (Figure 2b,c) to be 0.3 ± 0.1 nm, and thus indicating a monolayer. A proposed model of this monolayer is shown in Figure 2d where the side length of each molecule (indicated by red arrows) was estimated to be 3.9 nm, which is in excellent agreement with the lengths of **C4** molecules estimated from the AFM image (3.9 ± 0.1 nm). This rectangular pattern is greatly supported by the 2D FFT analysis (inset in Figure 2b) which shows repeating square units with a periodicity of 3.9 ± 0.1 nm in two directions, a distance that convincingly resembles the side lengths of the square structure of **C4**.

For the **C5**, no self-assembled domains could be observed by AFM investigation after spin-coating of a THF solution of this macrocycle onto HOPG. In the AFM images only agglomerates of the molecules were observed (Figure 3a). These clusters are formed probably due to a structural distortion of this cyclic molecule which impedes a planar conformation and thus a defined 2D-self-organization on HOPG surface in accordance with quantum chemical calculations (see below). On a closer look, however, few small domains could be observed in which a considerable number of single molecules are aligned next to each

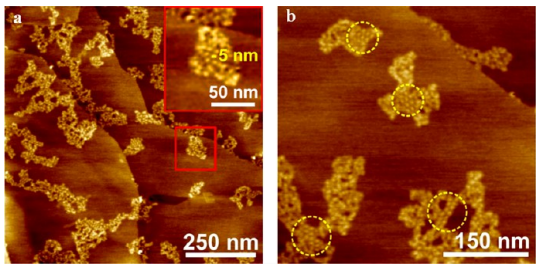

Figure 3. (a, b) AFM height images of C5 obtained by spin-coating from THF solution onto HOPG. Inset in panel a highlights one molecule of C5 (yellow line with 5 nm distance in red box).

other (highlighted with yellow dashed circles in Figure 3b). The height of these small assemblies was determined to be 0.4 ± 0.1 nm, indicating a monolayer (for a cross-section analysis, see Supporting Information, Figure S3). The diameter of one pentamer molecule was estimated to be 4.8 ± 0.6 nm and is therefore in a good agreement with the diameter of the planar model (4.7 ± 0.3 nm). But the interaction of the molecules with the HOPG surface seems to be in most cases too weak to flatten the molecule as corroborated by our quantum chemical calculations (see below).

A self-assembly of **C6** on HOPG was not observed by AFM investigation. After spin-coating from a $CHCl_3$ solution, only randomly distributed agglomerates with a height of about 1.8 ± 0.1 nm were revealed by AFM images (see Supporting Information, Figure S4). A structural distortion of this *CN* seems quite obvious for such a molecular size and will be shown in the following section by quantum chemical calculations. This increasing trend for distortion in going from **C3** to **C6** is greatly supported by the MD simulations as well as the photophysical properties at the single-molecule level which are described subsequently.

Molecular Dynamics Simulations. The results of the AFM measurements can be explained by an increasing flexibility of the cycles which is also in line with chemical intuition. To substantiate our view, we simulated variations in the geometrical structure and the intrinsic flexibilities of the cycles with increasing size. For this purpose we computed geometries and relative energies for some selected typical conformers and, to include all degrees of freedom, performed MD simulation. The *CN*s have various hinges which allow the reduction of ring strain. Model calculations for one unit (noncyclic acetylene-phenyl-PBI unit) predict that the torsional motion around (phenyl)C−N(PBI) bond possesses a quite flat potential with a barrier height of about 25 kJ/mol. This indicates that this motion will take place if it is not hindered by strain effects arising from the cyclization. This means that the conformers will be in the thermodynamical equilibrium. In contrast, the bending potential of the acetylene units is quite stiff. For a first rough overview, we investigated how the energy of *CN*s is influenced by the orientation

TABLE 1. Relative energies of the optimized structures; the starting structures are indicated

C3		C4		C5		C6	
a	*b*	*a*	*b*	*a*	*b*	*a*	*b*
ccc	0	tctc	0	tttcc	0	tctccc	0
tcc	36	ttcc	6	ttccc	2	ttttcc	3
ttc	59	cccc	8	tctcc	2	tttccc	4
ttt	53	tttc	12	cccc	5	tccccc	5
		tccc	13	ttttc	6	tcctcc	7
		tttt	18	tcccc	8	ttcccc	8
				ttctc	9	cccccc	11
				ttttt	14	ttctcc	11
						tctctc	11
						ttcttc	11
						ttttcc	13
						tttttt	13
						tttctc	15

[a] Starting structures by their sequences of *cis* (c) and *trans* (t) oriented acetylene linker. [b] Energy (kJ/mol).

of the acetylene linker with respect to the enclosed PBI moieties. All *cis* conformations give the formal rings but from chemical intuition *trans* orientation should become favorable for the larger rings. To get more solid information, we built up corresponding starting structures and performed geometry optimizations to the next local minimum. We used the PM6-DH2 approach[22] because model computations (see Supporting Information, Figure S6) indicate its reliability. To make these computations feasible, we omitted the phenoxy substituents because they should not possess too much influence. Table 1 gives the relative energies of the optimized structures while Figure 4 gives those optimized structures, which differ from the structure with the lowest energy by 10 kJ/mol or less. Table 1 characterizes the starting structures by their sequences of *cis* (c) and *trans* (t) oriented acetylene linker.

Our data underline the expected rigidity of **C3**. The geometry optimizations starting from structures which contain one *trans*-orientation lead to local minima which is 36 kJ/mol higher in energy than the minimum obtained from the ccc starting structure (Figure 4a). Please note that for this conformer one PBI unit is not perpendicular to the phenyl linker in the energy minimum. This might result because the conformer with three perpendicular PBI units is more strained. However, the potential for this torsional motion is rather flat (see Supporting Information, Figure S6) and accordingly it is likely that on the HOPG substrate all three PBI subunits lay flat and establish $\pi-\pi$-interactions with the substrate. Because the $S_0 \rightarrow S_1$ transition of PBI is polarized along the long molecular axis of the molecules, the optical properties and energy transfer processes among PBIs (see below) should be invariant to this rotational motion.

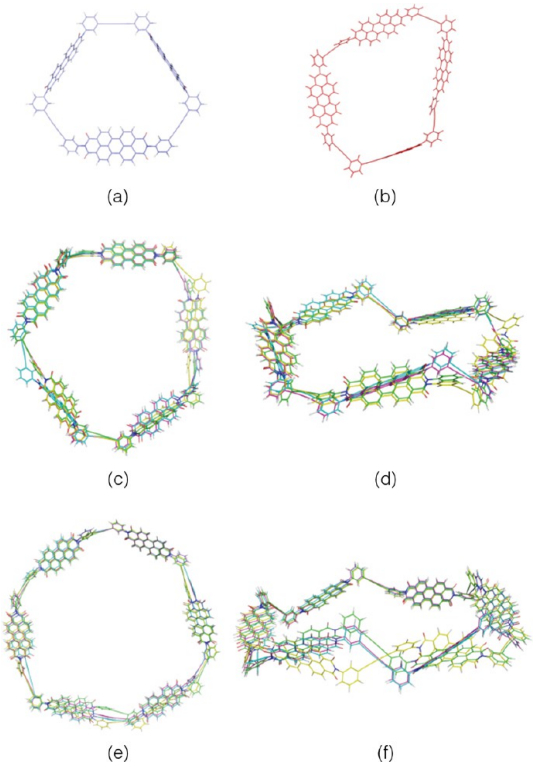

Figure 4. Sketch of optimized structures of (a) C3, (b) C4, (c) top view, and (d) side view of C5, (e) top view and (f) side view of C6. All shown conformations differ by less than 5 kJ/mol from the most stable structure.

The **C4** is slightly more flexible. The lowest lying conformer is obtained from the tctc starting structure (Figure 4b). The second lowest conformer (obtained ttcc) is already 6 kJ/mol higher in energy, that is, its population in the thermodynamic equilibrium is below 10%. Notably, the conformer that was obtained from the all *cis* starting structure is 8 kJ/mol higher in energy and thus even less populated. In the optimized structures of the tetramer, *cis*- and *trans*-oriented orientation can still be distinguished. As expected from the corresponding flat potential of the PBI-phenyl bond also in the tetramer, phenyl, and PBI units are not orthogonal to each other. While the **C3** ring is flat, the **C4** ring is already slightly nonplanar but might be flattened upon interaction of the PBI subunits with the HOPG substrate surface. The highly ordered large-size domains with square lattice suggest that this is indeed the case.

Starting from the possible orientations of the acetylene linker for the **C5**, we obtain four minima which differ by 5 kJ/mol or less from the lowest energy conformer. However, these minima strongly resemble each other, for example the acetylene linkers generally show *cis*-like orientations (Figure 4c) although the geometry optimization started from different orientations. For the **C6**, we also obtain three conformers, which are very similar (Figure 4e). In contrast, however, these structures contain both *cis*- and *trans*-oriented

structures. Like the **C5**, the **C6** forms a zigzag crown-like structure.

To explain the computational results, we have to take into account that an increased flexibility does not only diminish the energy differences between two conformers but also the barrier between them. For the **C3**, the high strain leads to large differences in the energy of the conformers. However, the barriers between two conformers are sufficiently high so that different starting structures lead to different local minima. This is also the case for the **C4** but due to the increasing flexibility the energy differences between the conformers decrease. The situation changes for **C5**. Because of the increased flexibility the barriers between possible conformers largely vanishes so that geometry optimizations starting from quite different orientations lead to very similar structures, which do not differ in the relative orientations of the acetylene linker. That for the **C5** *cis*-orientations are more favorable, while, for the **C6**, a mixture of *cis*- and *trans*-oriented units is preferred. In both cases, however, nonminimum structures are easily accessible by thermal energy at room temperature because of the flat potential energy surface.

Up to now the calculations only reflect parts of the flexibility because the number of starting structures is very small. They, furthermore, do not take into account possible influences of the phenoxy substituents. For further information we performed MD simulations for the complete systems using the PM6-DH2 approach and monitored the variation of geometrical parameters in the course of the MD simulations. Figure 5 which depicts the probability distribution for the occurrence of a dihedral angle between two PBI units obviously shows the increasing flexibility of the ring systems with increasing size. The **C3** rings only fluctuate around the planar all-*cis* conformation because strong strain effects prevent absolute values larger than 130° and keep the **C3** rings essentially flat. Already **C4** is considerably more flexible which is seen in the strong increase of the probability to take values of 180°. Nevertheless planar orientations with either *cis*- or *trans*-orientation belong still to the most favored geometries. The situation changes for **C5** and **C6**. Orientations with dihedral angles of 180° are now predominantly taken and the most abundant structures during the course of MD simulation resemble the nonplanar conformations as shown in Figure 4. Thus, our computations predict that **C5** and **C6** are considerably distorted during the course of the MD simulation.

The absence of well-ordered domains of **C5** and **C6** is easily explained by these computational results. On one hand, these two molecules show much more structural flexibility compared to their smaller counterparts. To form ordered domains on a surface this flexibility has to be reduced to a single conformation which is associated with a large entropic penalty.

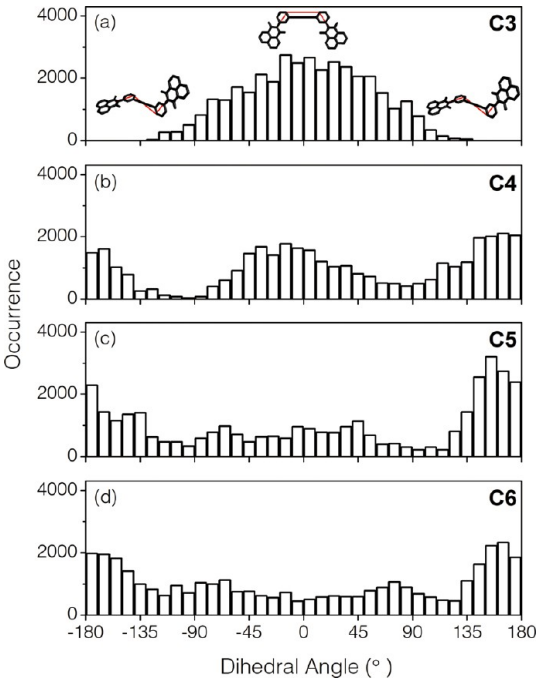

Figure 5. Distributions of the depicted dihedral angles during the course of the MD simulations performed with PM6-DH2. The ring size increases from (a) C3 to (d) C6.

On the other hand, both **C5** and **C6** adopt predominantly nonplanar geometries which will diminish the attractive interaction with the HOPG surface or, in other words, require a significant energetic penalty for the structural deformation into a planar structure.

Fluorescence Intensity Trajectories. To investigate the fluorescence dynamics of single *CN*s depending on the structural flexibility with increasing the ring size, SMS measurements were performed on immobilized *CN*s in polymeric matrix with a confocal microscope (TE2000-U, Nikon) by photoexcitation at 450 nm at room temperature under ambient conditions. Typical excitation power density was ~0.2 kW/cm^2. The sample films of *CN*s were prepared by spin-coating a toluene solution containing 10^{-10} M *CN* and 20 mg/mL PMMA.

As shown in Figure 6, *CN*s usually showed stepwise photobleaching. We have implemented the statistical analysis by collecting about 160 single-molecule FITs for each compound. Approximately, 53, 38, 29, and 19 % of the FITs of **C3**, **C4**, **C5**, and **C6**, respectively, exhibit stepwise photobleaching with the same number of intensity levels as the number of PBI chromophores in the corresponding compound. The remnants of the FITs present fewer intensity levels than the number of PBI units (Table 2) which may indicate either collective quenching (discussed below) or the presence of some chromophores in dark states already at the beginning of the FIT. The stepwise photobleaching indicates that *CN*s exhibit weak interactions between the PBI chromophores, as evidenced by other weakly coupled macrocycles.[49] In the previous ensemble

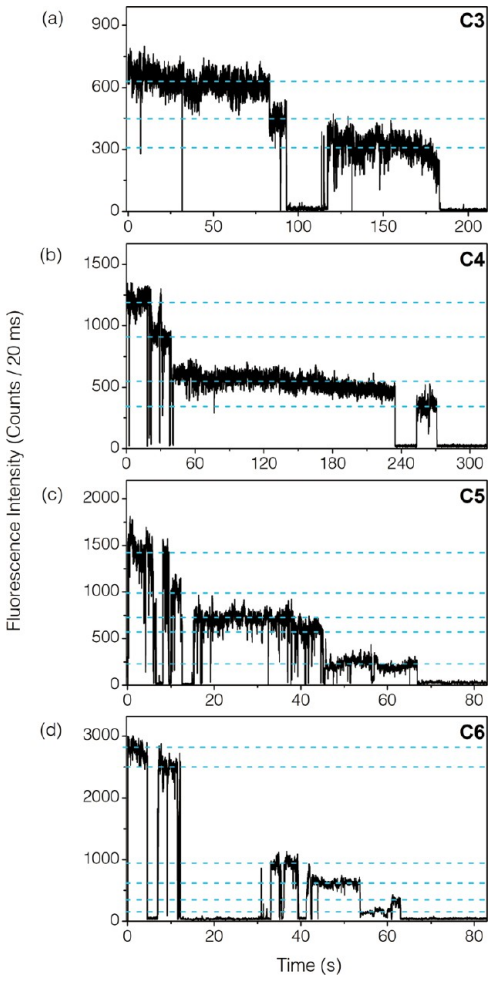

Figure 6. Stepwise photobleaching behaviors in the FITs of *CN*s in the polymer matrix at room temperature under ambient conditions: (a) 3-step photobleaching of C3, (b) 4-step photobleaching of C4, (c) 5-step photobleaching of C5, and (d) 6-step photobleaching of C6. The number of the blue lines in the FITs signifies the number of the intensity levels in the FITs.

study of *CN*s,[21] it was revealed that the absorption and fluorescence spectra of *CN*s are similar, and that the absorption coefficients monotonously increase in going from **M1** to **C6**. These results demonstrate that interactions between the PBI chromophores are weak, which is well matched with the stepwise photobleaching dynamics of *CN*s at the single-molecule level.

The important point to note is that we need to consider so-called collective blinking (or on/off) behavior which was observed in almost all FITs, that is, a temporal drop of fluorescence intensity to the background level (*e.g.*, at 31.7, 89.5, 93.1, 115.1, and 131.5 s with off-times of 0.04, 0.18, 21.96, 2.10, and 0.04 s, respectively, in Figure 6a). This blinking behavior is one of the characteristic features in single-molecule dynamics reflecting efficient EET to fluorescence quenching sites photogenerated in the system.[40] The collective quenching event can be due to direct Förster EET from an excited PBI to the quencher site formed

TABLE 2. The statistical analysis of the FITs of *CN*s

	the number of the intensity levels						
	1	2	3	4	5	6	ratio[a] (%)
C3	21	52	**83**				83/156 = 53%
C4	27	39	29	**59**			59/154 = 38%
C5	19	36	38	27	**48**		48/168 = 29%
C6	26	32	21	33	17	**31**	31/160 = 19%

[a] The ratio between the number of the FIT with the same number of the intensity levels as the number of the PBI units, and the number of the total FITs.

at one of PBIs,[41,42] or preceded by energy transfer between PBIs. The molecular size of *CN*s and the typical exciton quenching radius (3−5 nm)[41] are similar. As shown in Table 2, more than 50% of the FITs exhibit fewer intensity levels during photobleaching than the number of PBI units in the *CN*s. This is a clear indication of collective quenching. The table shows that the collective quenching is more pronounced for larger rings, which reflects considerable conformational heterogeneities by significant structural distortions. It is noteworthy that the fluorescence intensity trajectories of *CN*s at the single-molecule level provide the information on intramolecular interaction between the adjacent chromophores, that is, how the molecular system of *CN*s is photobleached, and the EET of *CN*s *via* collective blinking behaviors.

Fluorescence Lifetime and Photostability Measurements. We measured the fluorescence lifetimes of single *CN* molecules using TCSPC under excitation power of ~0.2 kW/cm^2. For every single-molecule, the fluorescence decay profile was constructed by fluorescence photons at the first emissive level in the FITs and fitted by a single exponential function. Figure 7 shows the histograms of the fluorescence lifetimes of *CN*s at the single-molecule level, and the solid lines in the histograms correspond to the fitted Gaussian distribution functions with the average fluorescence lifetimes of 7.0, 6.6, 6.4, and 6.5 ns for **C3**, **C4**, **C5**, and **C6**, respectively. The full width at half-maximum (fwhm) values of the solid lines are 1.48 ± 0.06, 1.53 ± 0.08, 1.62 ± 0.07, and 2.92 ± 0.19 ns for **C3**, **C4**, **C5**, and **C6**, respectively. The trend of the decreasing fluorescence lifetimes with an increase of the size of *CN*s was also observed at the ensemble level; 6.6, 6.1, 6.0, and 5.8 ns for **C3**, **C4**, **C5**, and **C6**, respectively.[21] As the size of *CN*s increases, it is likely that the structural flexibility in the cyclic molecular structures increases. Thus, the structures of large *CN*s become distorted, leading to an increase of the conformational heterogeneity, as illustrated above by the AFM height images and the MD simulations. As a result, the structural distortion opens up new radiationless deactivation channels shortening of the fluorescence lifetime. The fluorescence lifetimes in toluene are slightly shorter than those at the single-molecule level in PMMA. This discrepancy originates from an

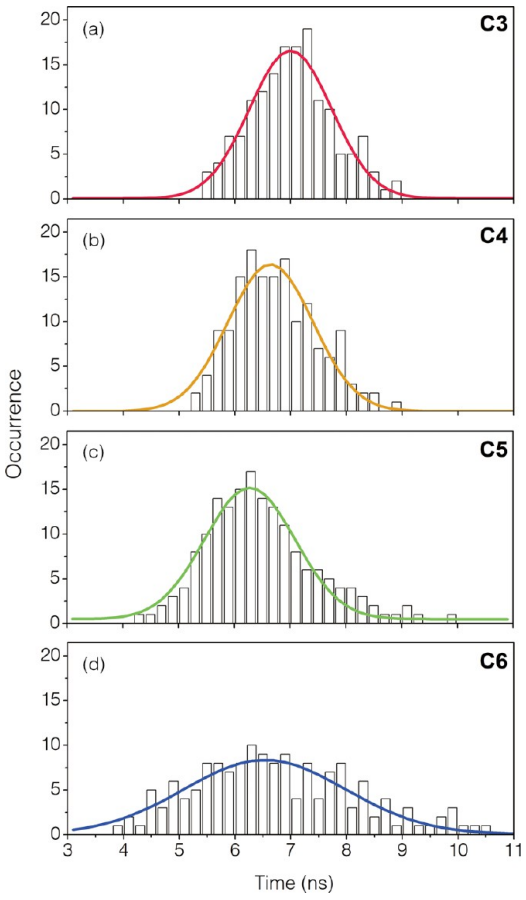

Figure 7. Fluorescence lifetime distributions of *CN*s in 20 mg/mL PMMA matrix. The histograms were fitted by a Gaussian function. (a) $\tau = 7.0$ ns, fwhm $= 1.48 \pm 0.06$ ns of C3, (b) $\tau = 6.6$ ns, fwhm $= 1.53 \pm 0.08$ ns of C4, (c) $\tau = 6.4$ ns, fwhm $= 1.62 \pm 0.07$ ns of C5, and (d) $\tau = 6.5$ ns, fwhm $= 2.92 \pm 0.19$ ns of C6.

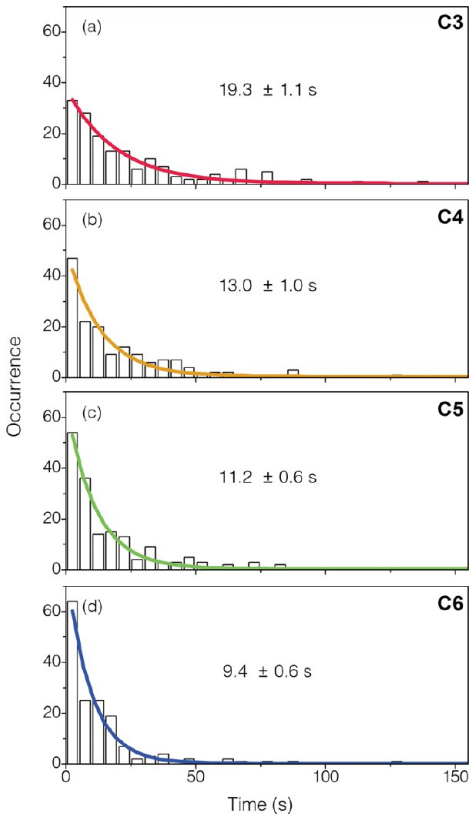

Figure 8. Histograms of the on-times at the first intensity levels in the FITs of *CN*s in 20 mg/mL PMMA matrix. The on-times of 19.3 ± 1.1, 13.0 ± 1.0, 11.2 ± 0.6, and 9.4 ± 0.6 s for C3, C4, C5, and C6 were fitted by a single exponential function.

environmental difference between the solution and the condensed state.

As shown in Figure 7, the fluorescence lifetime distributions of *CN*s become broader with an increase in the number of PBI units. We assume that the larger the size of the *CN* is, the more the conformational heterogeneity increases due to the structural distortions. As seen in the cross-section analysis (Supporting Information, Figure S4c) and the optimized structures showing the mixture of *cis*- and *trans*-orientations (Figure 4e,f) of **C6**, it is likely that the structures of **C6** are the most distorted among the studied PBI macrocycles. In contrast, the structures of **C3** are nearly flat in agreement with the height of **M1** (for the AFM image in Supporting Information, Figure S5) and the MD simulations (Figure 4a and 5a). Therefore, the broader distribution of the fluorescence lifetimes of **C6** clearly corroborates that there are significant structural heterogeneities.

Next, we have examined the photostability of *CN*s in the PMMA polymer matrix under continuous photoexcitation at the excitation power of ~0.2 kW/cm^2. The on-time of the first fluorescence intensity level in the FITs can be strongly associated with the photostability of single molecules under photoexcitation since this level reflects the intrinsic status of the molecules prior to any photoinduced damage. Figure 8 shows the histograms of the on-times at the first intensity level of *CN*s. The histograms were fitted by single exponential decay function with the time constants of 19.3 ± 1.1, 13.0 ± 1.0, 11.2 ± 0.6, and 9.4 ± 0.6 s for **C3**, **C4**, **C5**, and **C6**, respectively. The on-times at the first intensity levels become shorter with increasing the ring size, which indicates that the photostability weakens. This feature may be connected to the increased structural flexibility of the larger rings which makes photochemical reactions more efficient than in the rigid and well-defined structure of **C3**. This phenomenon is also observed in other chlorophyll multichromophoric systems with relatively short and long linkers.[33] Even the number of the chromophores in the molecular systems is the same, the on-times at the first intensity levels decrease with an increase of the structural flexibility in the molecular system with long linker. Thus, it is thought that the photostability of *CN*s can be affected by the distorted geometries which show photochemical reactions.

Additionally, since the larger ring systems absorb more light at the given excitation power, the probability

to create photochemical processes increases. Then, combined with the collective bleaching, the larger systems can be photobleached faster. It actually fits with the experimental results (Figure 8). **C6** has two times more chromophores than **C3**, and it survives two times less in its first emitting level.

Fluorescence Polarization Measurements. Fluorescence polarization measurements at the single-molecule level[50−54] are very useful for understanding quenching processes and energy transfer in multichromophoric systems.[55,56] *CN*s were excited by circularly polarized light with an excitation power of ~0.2 kW/cm^2. We used a polarized beam splitter to separate parallel-polarized (*s*) and perpendicular-polarized (*p*) components of the emitted light, and each of these components was detected with two independent APD detectors. The change in the relative intensity of the two channels is illustrated by the change in the steady-state polarization *P*, which is defined as

$$P = \frac{A - GB}{A + GB}$$

Where *A* and *B* are intensities of *s*- and *p*-components of the fluorescence light and *G* is the correction factor to account for differences in the detection efficiencies of the two channels.

Figure 9 displays the representative polarization trajectories of **C3** and **C4** along with their FITs. The polarization trajectories can be roughly classified into two types. In the trajectories of the first type, the value of *P* is changing when the stepwise photobleaching occur (Figure 9a,b), whereas the trajectories of the second type show a constant polarization level irrespective of photobleaching (Figure 9c,d). We assume that the fluorescence of *CN*s always comes from a low-energy subset of PBIs. In the first case bleaching of one or more PBIs obviously changes this subset and, due to different orientations of the PBIs in the rings, leads to changes in the polarization degree. For example, if such situation would be realized due to efficient EET, the emission was coming just from a single emitting trap and this trapping PBI was bleached. The bleached trap was then replaced by another PBI possessing different orientation resulting in a different *P* value. The trajectories of the second type (Figure 9c,d) can occur if the observed emission is coming from a single emitting trap[51] while the other PBIs work as a LH antenna and do not emit light by themselves.[56] This is another evidence of EET processes between PBIs in *CN*s at the single-molecule level. The statistical analysis shows that the probability for the *CN* to possess stable fluorescence polarization (case two) decreases with the increase of *CN*'s size and is equal to 51, 45, 28, and 26% for **C3**, **C4**, **C5**, and **C6**, respectively. It is more difficult for **C5** and **C6** to possess a stable single emitting site probably because of the more distorted (and possibly flexible) structures and larger number of PBI units.

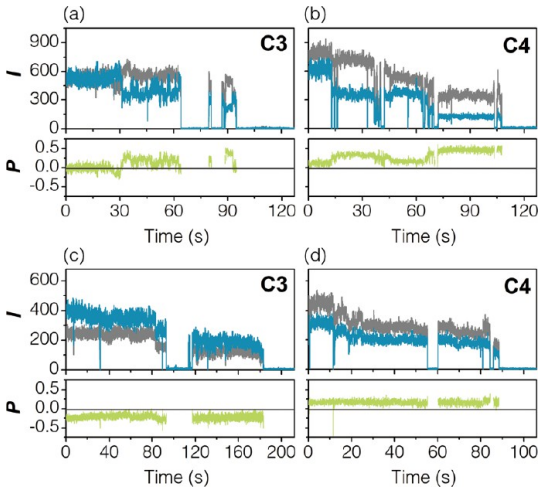

Figure 9. Representative polarization trajectories (green lines) of C3 and C4 with the stepwise photobleaching behavior in the FITs (gray line is *s*-polarization component and blue is *p*-polarization component). *I* represents the number of photon counts per 20 ms. (a) A changing level in polarization trajectory with 3-step photobleaching behavior of C3, (b) a changing level in polarization trajectory with 4-step photobleaching behavior of C4, (c) a constant level in polarization trajectory with 3-step photobleaching behavior of C3, (d) a constant level in polarization trajectory with 4-step photobleaching behavior of C4.

Indeed, the types of the polarization trajectories of **C5** and **C6** were considerably complicated. It is thought that various types of the polarization trajectories in larger systems are significantly affected by their structural distortions.

Coincidence Measurements. We carried out coincidence measurements to evaluate the EET efficiency of **C3**, **C4**, **C5**, and **C6** *via* observation of singlet−singlet (S_1-S_1) exciton annihilation.[57] This process occurs when two or more singlet excitons are generated by a short laser pulse making possible the following reaction: $S_1 + S_1 \rightarrow S_0 + S_n \rightarrow S_0 + S_1 +$ heat. As a result, one exciton disappears (the excited molecule returns to S_0) while the other remains after fast internal conversion from S_n to S_1. Because it requires the excitons to collide or at least be close to each other, exciton migration is needed for the annihilation to occur. Thus we can use annihilation as a measure of the EET efficiency among PBI units in the cyclic PBI arrays.

We have chosen the molecules which keep all chromophores active at the first emissive level. Photons arrived during this first intensity level were then used for analysis. An example of such a molecule is the **C3** molecule shown in Figure 10a. It possessed three intensity levels during photobleaching and all three chromophores were active in the beginning of the FIT (the first 0.6 s in Figure 10a). In Figure 10b, the distances between the peaks are 100 ns corresponding to the inverse laser pulse repetition rate. The peak at $t = 1000$ ns (the time scale is relative) gives the number of the coincident photon pairs (N_C). All other peaks give the number of photon pairs when individual photons are

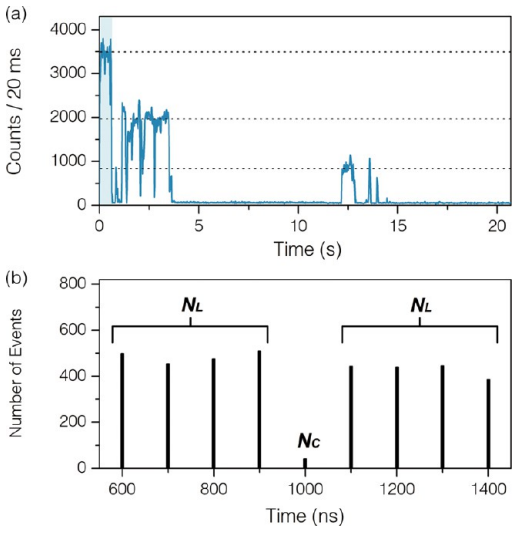

Figure 10. (a) The 3-step photobleaching FIT of C3. (b) The corresponding interphoton arrival time distribution of C3. (N_C and N_L signify central (coincidence events) and lateral peaks, respectively, see the text for details).

originated from different excitation pulses (N_L) that is proportional to the fluorescence intensity of the molecules. The N_C/N_L ratio can be used to estimate the number of independently emitting chromophores. Neglecting background signals, the N_C/N_L values of 0.0, 0.5, 0.67, and 0.75 are expected for one, two, three, and four emitters, respectively.[58] The smaller is the value of N_C/N_L, the more efficient S_1-S_1 annihilation and EET processes are.[59,60]

For all *CN*s, we have evaluated the N_C/N_L values for the single molecules; 50 single-molecule data sets were employed for each array. As shown in Figure 11, the average N_C/N_L values are 0.06, 0.08, 0.10, and 0.11 for **C3**, **C4**, **C5**, and **C6**, respectively. With an increase in the size of *CN*s, their average N_C/N_L values become gradually larger, and the N_C/N_L distributions become broader. In our experimental conditions (signal/background $\approx$ 70), the single emitting chromophore situation should give N_C/N_L = 0.06.[39,58] This value is very close to that observed for **C3**. This implies that **C3** exhibits a very high energy transfer efficiency supported by its well-defined and rigid planar structure.

Generally, the EET highly depends on the spectral overlap of the molecular system, the relative orientation of the transient dipoles, and the distance between the interacting chromophores.[61] Since the absorption and fluorescence spectra of *CN*s are similar regardless of the ring size (absorption λ_{max} = around 583 nm, and fluorescence λ_{max} = 614 nm in Supporting Information, Figure S7), the EET efficiency is not affected by the spectral overlap of *CN*s. However, considering the ring sizes of 2.5, 3.2, 3.9, and 4.7 nm averaged from MD simulations (the maximal distance between two carbon atoms of the imide-bonding) for **C3**, **C4**, **C5**, and **C6**, respectively, the distances between the interacting

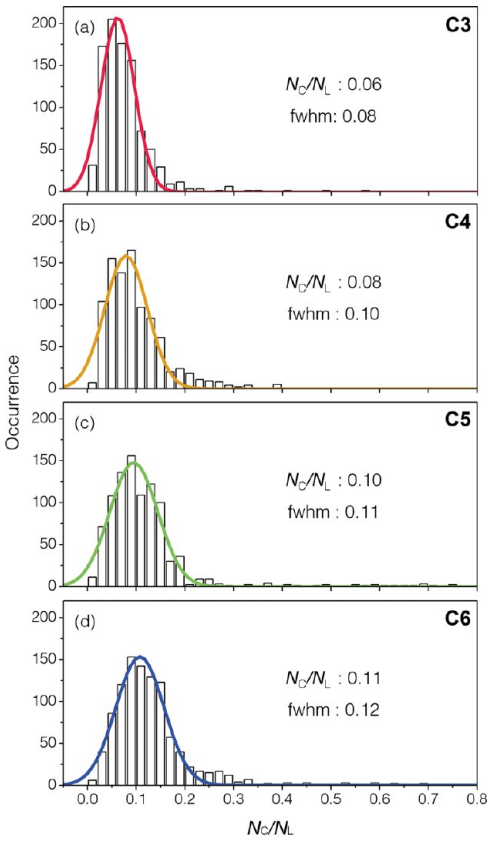

Figure 11. Histograms of the N_C/N_L values of *CN*s collected from 50 single-molecule data sets for each array. All histograms were fitted with a Gaussian distribution function.

chromophores and the angles of their transition dipoles are varied with increasing ring size. Even the structural distortion becomes larger in larger cyclic systems. Consequently, we assume that the distinct differences in the structures of *CN*s with increasing the ring size have influence on the EET efficiency. The smaller N_C/N_L value for **C3** than those for **C4**, **C5**, and **C6** indicates that **C3** can be considered as a well-defined and planar cyclic structure for efficient EET processes. On the other hand, the more structural distortion in a larger **C6** system might reduce the EET efficiency by introducing competitive nonradiative decay channels. As shown in the histograms of the fluorescence lifetimes of *CN*s in Figure 7, the fluorescence lifetime distributions become broader with the reduction of fluorescence lifetimes in larger systems. These results are induced by the conformational flexibility in larger systems leading to more structural distortions with radiationless deactivation channels. In accordance with this feature, N_C/N_L distributions become broader with the increase of the ring size by the conformational heterogeneities. It is demonstrated that the EET efficiency in *CN*s is determined from their structural distortions.

Although the N_C/N_L value clearly increases with increasing the ring size, it is still much less than that

for two emitting sites (0.5). So, we conclude that PBI arrays from **C3** to **C6** behave, to a large extent, as single photon emitters. The reason for a slight decrease of the exciton annihilation in large rings is not very clear because even the largest PBI array (**C6**) is still a very compact system where efficient annihilation is expected. However, as our AFM studies and calculations showed, large rings (**C5** and **C6**) can possess distorted structures. Because of distortions and, consequently, increased energetic disorder, the formation of two distinct exciton traps (emitting sites) well separated in space by several nanometers seems possible. In such cases, interaction between the two S_1 excitons populating the traps may not be strong enough to completely exclude photon coincidence events.

It is also interesting that N_C/N_L distributions become broader with the increase of the ring size. It means that for the large rings the exciton annihilation efficiency (and EET) varies from molecule to molecule (due to, for example, differences in their geometries) and also probably fluctuates during the data acquisition time which was of the order of 0.6 s (Figure 10a).

CONCLUSIONS

The macrocycles of acetylene linked PBI cyclic arrays (*CN*s) have been investigated by atomic force microscopy (AFM) and single-molecule fluorescence spectroscopy with a focus on the influences of the overall structural rigidity on the efficiency of excitation energy transfer (EET) processes with increasing size of *CN*s. It is clearly shown by the AFM height images on highly ordered pyrolytic graphite surface and molecular dynamics (MD) simulations that the structures of *CN*s become more distorted in going from **C3** to **C6**. All together our computational results explain AFM and the single-molecule spectroscopy data. At ambient temperatures **C3** and **C4** form essentially one conformer because all other conformers are considerably higher in energy. Because of this rigidity the formation of highly ordered domains became possible, whereas the high flexibility and the prevalence of nonplanar conformations precluded the formation of such domains for **C5** and **C6**. The increasing flexibility indicated by our computations rationalizes the single molecule data which show that the distributions of photophysical parameters considerably broaden if one goes to the larger ring systems. At the single-molecule level, the smaller rings (**C3** and **C4**) show higher photostability and EET efficiency than the larger molecules due to relatively rigid and well-defined structures of the **C3** and **C4** in comparisons to **C5** and **C6**. These results demonstrate that the small rigid macrocycles without structural distortion are optimal to show effective light-harvesting (LH) and stability at the same time. Even though more pigments incorporated in the larger cyclic arrays enable to increase the light absorption capability, it does not necessarily lead to higher LH efficiency. Larger rings are more susceptible to photochemical degradation and, structural distortions followed by overall structural flexibility deteriorating the EET resulting in inefficient LH. The overall rigidity in the molecular structures is a primary factor to obtain efficient and robust artificial LH systems in the solid state.

METHODS

Ensemble Spectroscopy. Steady-state absorption and fluorescence (580 nm excitation wavelength) of *CN*s in toluene (Aldrich, spectrophotometric grade) were measured using a Cary5000 (Varian) UV/vis spectrometer and F-2500 (Hitachi) fluorometer.

Sample Preparation. The synthesis of *CN*s has been described previously.[20] Samples for SMS measurements were prepared by spin-coating solutions of *CN*s ($\sim 10^{-10}$ M) in toluene containing 20 mg/mL PMMA (Aldrich, average M.W. = 96 700) on rigorously cleaned quartz coverslips at 2000 rpm for 50 s. Thickness of the obtained PMMA films doped by *CN*s was ~100 nm as measured by AFM.

Atomic Force Microscopy. AFM investigations were performed under ambient conditions using a MultiMode Nanoscope IV system (Bruker AXS, Santa Barbara, CA), operating in a tapping mode in air. Silicon cantilevers (Olympus, Japan) with a resonance frequency of ~300 kHz and spring constant of ~42 N/m were used. Samples were prepared by spin-coating of a 7.5×10^{-6} M solution of each of these macrocycles onto HOPG.

Single-Molecule Fluorescence Spectroscopy. Detection of single-molecule fluorescence was performed with a confocal microscope (TE2000-U, Nikon) equipped with a sample scanning stage (XE-120, Park Systems) at room temperature under ambient conditions. The sample was excited by a circularly polarized light from a picosecond pulsed diode laser (LDH-D-C-450, Picoquant, 450 nm, 10 MHz repetition rate, 70 ps pulse width) prepared by a Berek compensator (5540, New Focus). The laser beam was focused onto the sample *via* an oil immersion objective lens (Plan Fluor, 1.3 NA, 100×, Nikon) giving irradiation power of ~0.2 kW/cm^2 at the sample. Fluorescence was collected using the same objective, passed through a dichroic mirror (z457rdc, Chroma Technology), filtered with a notch filter (HNPF-450.0−1.0, Kaiser Optical Systems Inc.) as well as long pass filters (HQ488lp and HQ500lp, Chroma Technology), and focused on an avalanche photodiode (APD) (SPCM-AQR-16-FC, EG&G). After an individual molecule was positioned in the laser focus, the fluorescence signal detected by the APD was registered by a time-correlated single photon counting (TCSPC) PC card (SPC 830, Becker & Hickl) operated in first-in-first-out regime, in which the arrival time after the beginning of the acquisition and the time lag with respect to the excitation pulse were stored for each detected photon. The fwhm of the overall instrumental response function was about 500−600 ps. These data were processed using BIFL data analyzer software (Scientific Software Technologies Center) to obtain the FITs with a user-defined binning time, and the time-resolved fluorescence decays using photons belonging to a user-defined region in the trajectories.

For the fluorescence polarization measurement, we used a polarization beam splitter (PBS101, Thorlabs) to separate parallel- and perpendicular-polarized components of the emitted light which were detected by two independent APDs.

Coincidence Measurements. For the coincidence measurements, a classical Hanbury-Twiss and Brown type of setup (the coincidence setup)[39,58] in combination with pulsed excitation

(the excitation power was ≈ 2 kW/cm^2) was used. For this purpose a 50:50 nonpolarizing beam splitter was added in the detection part such that the fluorescence was focused on two APD detectors. The signals from both APDs were fed into a router of TCSPC PC card (SPC 830, Becker & Hickl), and one of the two signals was delayed by applying electronic delay (915.5 ns). This procedure allows detection of multiple fluorescence photons generated by the same laser pulse. A time-to-amplitude converter measured the time intervals between photons (one detector channel was the start, and the other was the stop). Because we used pulsed excitation light, the histogram of the interphoton arrival times is determined by the laser repetition rate (10 MHz).

Molecular Dynamics Simulations. The MD simulations contained 60 000 time steps of 1 fs from which 600 frames were used in the analyses. The simulations were performed for 300 K using a Nose–Hoover thermostat. All calculations were conducted with the in-house CAST program package.

Conflict of Interest: The authors declare no competing financial interest.

Acknowledgment. The work at Yonsei University was financially supported by the Midcareer Researcher Program (2010-0029668) of the National Research Foundation (NRF) grant funded by the Ministry of Education, Science, and Technology (MEST) of Korea. The work at the University of Würzburg was supported by the DFG in the framework of the research unit "Light-induced dynamics in molecular aggregates". I.G. Scheblykin thanks the Knut & Alice Wallenberg Foundation.

Supporting Information Available: Additional AFM images, computations, absorption and fluorescence spectra. This material is available free of charge *via* the Internet at http://pubs.acs.org.

REFERENCES AND NOTES

1. Pullerits, T.; Sundström, V. Photosynthetic Light-Harvesting Pigment–Protein Complexes: Toward Understanding How and Why. *Acc. Chem. Res.* **1996**, *29*, 381–389.
2. Roszak, A. W.; Howard, T. D.; Southall, J.; Gardiner, A. T.; Law, C. J.; Isaacs, N. W.; Cogdell, R. J. Crystal Structure of the RC-LH1 Core Complex from *Rhodopseudomonas palustris*. *Science* **2003**, *302*, 1969–1972.
3. Aratani, N.; Kim, D.; Osuka, A. Discrete Cyclic Porphyrin Arrays as Artificial Light-Harvesting Antenna. *Acc. Chem. Res.* **2009**, *42*, 1922–1934.
4. Yang, J.; Yoon, M.-C.; Yoo, H.; Kim, P.; Kim, D. Excitation Energy Transfer in Multiporphyrin Arrays with Cyclic Architectures: Towards Artificial Light-Harvesting Antenna Complexes. *Chem. Soc. Rev.* **2012**, *41*, 4808–4826.
5. Anderson, S.; Anderson, H. L.; Sanders, J. K. M. Expanding Roles for Templates in Synthesis. *Acc. Chem. Res.* **1993**, *26*, 469–475.
6. Li, J.; Ambroise, A.; Yang, S. I.; Diers, J. R.; Seth, J.; Wack, C. R.; Bocian, D. F.; Holten, D.; Lindsey, J. S. Template-Directed Synthesis, Excited-State Photodynamics, and Electronic Communication in a Hexameric Wheel of Porphyrins. *J. Am. Chem. Soc.* **1999**, *121*, 8927–8940.
7. Nakao, K.; Nishimura, M.; Tamachi, T.; Kuwatani, Y.; Miyasaka, H.; Nishinaga, T.; Iyoda, M. Giant Macrocycles Composed of Thiophene, Acetylene, and Ethylene Building Blocks. *J. Am. Chem. Soc.* **2006**, *128*, 16740–16747.
8. Iyoda, M.; Yamakawa, J.; Rahman, M. J. Conjugated Macrocycles: Concepts and Applications. *Angew. Chem., Int. Ed.* **2011**, *50*, 10522–10553.
9. Zhang, W.; Moore, J. S. Shape-Persistent Macrocycles: Structures and Synthetic Approaches from Arylene and Ethynylene Building Blocks. *Angew. Chem., Int. Ed.* **2006**, *45*, 4416–4439.
10. Jester, S.-S.; Sigmund, E.; Höger, S. J. Nanopatterning by Molecular Polygons. *J. Am. Chem. Soc.* **2011**, *133*, 11062–11065.
11. Gross, D. E.; Moore, J. S. Arylene–Ethynylene Macrocycles *via* Depolymerization-Macrocyclization. *Macromolecules* **2011**, *44*, 3685–3687.
12. Gholami, M.; Tykwinski, R. R. Oligomeric and Polymeric Systems with a Cross-Conjugated π-Framework. *Chem. Rev.* **2006**, *106*, 4997–5027.
13. Lang, E.; Hildner, R.; Engelke, H.; Osswald, P.; Würthner, F.; Köhler, J. Comparison of the Photophysical Parameters for Three Perylene Bisimide Derivatives by Single-Molecule Spectroscopy. *ChemPhysChem* **2007**, *8*, 1487–1496.
14. Zang, L.; Liu, R.; Holman, M. W.; Nguyen, K. T.; Adams, D. M. A Single-Molecule Probe Based on Intramolecular Electron Transfer. *J. Am. Chem. Soc.* **2002**, *124*, 10640–10641.
15. Würthner, F.; Stolte, M. Naphthalene and Perylene Diimides for Organic Transistors. *Chem. Commun.* **2011**, *47*, 5109–5115.
16. Wang, C.; Dong, H.; Hu, W.; Liu, Y.; Zhu, D. Semiconducting π-Conjugated Systems in Field-Effect Transistors: A Material Odyssey of Organic Electronics. *Chem. Rev.* **2012**, *112*, 2208–2267.
17. Law, K.-Y. Organic Photoconductive Materials: Recent Trends and Developments. *Chem. Rev.* **1993**, *93*, 449–486.
18. Zhan, X.; Facchetti, A.; Barlow, S.; Marks, T. J.; Ratner, M. A.; Wasielewski, M. R.; Marder, S. R. Rylene and Related Diimides for Organic Electronics. *Adv. Mater.* **2011**, *23*, 268–284.
19. Wasielewski, M. R. Self-Assembly Strategies for Integrating Light Harvesting and Charge Separation in Artificial Photosynthetic Systems. *Acc. Chem. Res.* **2009**, *42*, 1910–1921.
20. Schlosser, F.; Stepanenko, V.; Würthner, F. Perylene Bisimide Macrocycles and Their Self-Assembly on HOPG Surfaces. *Chem. Commun.* **2010**, *46*, 8350–8352.
21. Schlosser, F.; Sung, J.; Kim, P.; Kim, D.; Würthner, F. Excitation Energy Migration in Covalently Linked Perylene Bisimide Macrocycles. *Chem. Sci.* **2012**, *3*, 2778–2785.
22. Stewart, J. J. P. *MOPAC2012*, version 13.064L; Stewart Computational Chemistry: Colorado Springs, CO, 2012, http://OpenMOPAC.net.
23. Métivier, R.; Nolde, F.; Müllen, K.; Basché, T. Electronic Excitation Energy Transfer between Two Single Molecules Embedded in a Polymer Host. *Phys. Rev. Lett.* **2007**, *98*, 047802.
24. Schlichting, P.; Duchscherer, B.; Seisenberger, G.; Basché, T.; Bräuchle, C.; Müllen, K. A Bichromophore Based on Perylene and Terrylene for Energy Transfer Studies at the Single-Molecule Level. *Chem.—Eur. J.* **1999**, *5*, 2388–2395.
25. Lang, E.; Würthner, F.; Köhler, J. Photophysical Properties of a Tetraphenoxy-Substituted Perylene Bisimide Derivative Characterized by Single-Molecule Spectroscopy. *ChemPhysChem* **2005**, *6*, 935–941.
26. Krause, S.; Aramendia, P. F.; Täuber, D.; von Borczyskowski, C. Freezing Single Molecule Dynamics on Interfaces and in Polymers. *Phys. Chem. Chem. Phys.* **2011**, *13*, 1754–1761.
27. Yoo, H.; Furumaki, S.; Yang, J.; Lee, J.-E.; Chung, H.; Oba, T.; Kobayashi, H.; Rybtchinski, B.; Wilson, T. M.; Wasielewski, M. R.; et al. Excitonic Coupling in Linear and Trefoil Trimer Perylenediimide Molecules Probed by Single-Molecule Spectroscopy. *J. Phys. Chem. B* **2012**, *116*, 12878–12886.
28. Lounis, B.; Moerner, W. E. Single Photons on Demand from a Single Molecule at Room Temperature. *Nature* **2000**, *407*, 491–493.
29. Moerner, W. E. A Dozen Years of Single-Molecule Spectroscopy in Physics, Chemistry, and Biophysics. *J. Phys. Chem. B* **2002**, *106*, 910–927.
30. Kulzer, F.; Orrit, M. Single-Molecule Optics. *Annu. Rev. Phys. Chem.* **2004**, *55*, 585–611.
31. Tinnefeld, P.; Sauer, M. Branching out of Single-Molecule Fluorescence Spectroscopy: Challenges for Chemistry and Influence on Biology. *Angew. Chem., Int. Ed.* **2005**, *44*, 2642–2671.
32. Wöll, D.; Braeken, E.; Deres, A.; De Schryver, F. C.; Uji-I, H.; Hofkens, J. Polymers and Single Molecule Fluorescence Spectroscopy, What Can We Learn?. *Chem. Soc. Rev.* **2009**, *38*, 313–328.
33. Lee, J.-E.; Yang, J.; Gunderson, V. L.; Wasielewski, M. R.; Kim, D. Fluorescence Dynamics of Chlorophyll Trefoils in the Solid State Studied by Single-Molecule Fluorescence Spectroscopy. *J. Phys. Chem. Lett.* **2010**, *1*, 284–289.

34. Lee, J.-E.; Yang, J.; Kim, D. Single-Molecule Fluorescence Dynamics of a Butadiyne-Linked Porphyrin Dimer: The Effect of Conformational Flexibility in Host Polymers. *Faraday Discuss.* **2012**, *155*, 277–288.
35. Hernando, J.; Hoogenboom, J. P.; van Dijk, E. M. H. P.; García-López, J. J.; Crego-Calama, M.; Reinhoudt, D. N.; van Hulst, N. F.; García-Parajó, M. F. Single Molecule Photobleaching Probes the Exciton Wave Function in a Multichromophoric System. *Phys. Rev. Lett.* **2004**, *93*, 236404.
36. Yang, J.; Yoo, H.; Aratani, N.; Osuka, A.; Kim, D. Determination of the Superradiance Coherence Length of Directly Linked Linear Porphyrin Arrays at the Single-Molecule Level. *Angew. Chem., Int. Ed.* **2009**, *48*, 4323–4327.
37. Vacha, M.; Koide, Y.; Kotani, M.; Sato, H. Single Molecule Detection and Photobleaching Study of a Phosphorescent Dye: Organometallic Iridium(III) Complex. *Chem. Phys. Lett.* **2004**, *388*, 263–268.
38. Issac, A.; Hildner, R.; Ernst, D.; Hippius, C.; Würthner, F.; Köhler, J. Single Molecule Studies of Calix[4]arene-Linked Perylene Bisimide Dimers: Relationship between Blinking, Lifetime and/or Spectral Fluctuations. *Phys. Chem. Chem. Phys.* **2012**, *14*, 10789–10798.
39. Tinnefeld, P.; Weston, K. D.; Vosch, T.; Cotlet, M.; Weil, T.; Hofkens, J.; Müllen, K.; De Schryver, F. C.; Sauer, M. Antibunching in the Emission of a Single Tetrachromophoric Dendritic System. *J. Am. Chem. Soc.* **2002**, *124*, 14310–14311.
40. Vanden Bout, D. A.; Yip, W.-T.; Hu, D.; Fu, D.-K.; Swager, T. M.; Barbara, P. F. Discrete Intensity Jumps and Intramolecular Electronic Energy Transfer in the Spectroscopy of Single Conjugated Polymer Molecules. *Science* **1997**, *277*, 1074–1077.
41. Scheblykin, I. G.; Zoriniants, G.; Hofkens, J.; De Feyter, S.; Van der Auweraer, M.; De Schryver, F. C. Photoluminescence Intensity Fluctuations and Electric-Field-Induced Photoluminescence Quenching in Individual Nanoclusters of Poly(phenylenevinylene). *ChemPhysChem* **2003**, *4*, 260–267.
42. Mirzov, O.; Cichos, F.; von Borczyskowski, C.; Scheblykin, I. G. Direct Exciton Quenching in Single Molecules of MEH-PPV at 77 K. *Chem. Phys. Lett.* **2004**, *386*, 286–290.
43. Elemans, J. A. A. W.; Lei, S.; De Feyter, S. Molecular and Supramolecular Networks on Surfaces: From Two-Dimensional Crystal Engineering to Reactivity. *Angew. Chem., Int. Ed.* **2009**, *48*, 7298–7332.
44. Ciesielski, A.; Palma, C.-A.; Bonini, M.; Samorì, P. Towards Supramolecular Engineering of Functional Nanomaterials: Pre-Programming Multi-Component 2D Self-Assembly at Solid−Liquid Interfaces. *Adv. Mater.* **2010**, *22*, 3506–3520.
45. Gutzler, R.; Cardenas, L.; Rosei, F. Kinetics and Thermodynamics in Surface-Confined Molecular Self-Assembly. *Chem. Sci.* **2011**, *2*, 2290–2300.
46. Würthner, F. Perylene Bisimide Dyes as Versatile Building Blocks for Functional Supramolecular Architectures. *Chem. Commun.* **2004**, 1564–1579.
47. Chen, Z.; Lohr, A.; Saha-Möller, C. R.; Würthner, F. Self-Assembled π-Stacks of Functional Dyes in Solution: Structural and Thermodynamic Features. *Chem. Soc. Rev.* **2009**, *38*, 564–584.
48. Chen, Z.; Baumeister, U.; Tschierske, C.; Würthner, F. Effect of Core Twisting on Self-Assembly and Optical Properties of Perylene Bisimide Dyes in Solution and Columnar Liquid Crystalline Phases. *Chem.—Eur. J.* **2007**, *13*, 450–465.
49. Park, M.; Yoon, M.-C.; Yoon, Z. S.; Hori, T.; Peng, X.; Aratani, N.; Hotta, J.-I.; Uji-I, H.; Sliwa, M.; Hofkens, J.; Osuka, A.; Kim, D. Single-Molecule Spectroscopic Investigation of Energy Migration Processes in Cyclic Porphyrin Arrays. *J. Am. Chem. Soc.* **2007**, *129*, 3539–3544.
50. Sliwa, M.; Flors, C.; Oesterling, I.; Hotta, J.-I; Müllen, K.; De Schryver, F. C.; Hofkens, J. Single Perylene Diimide Dendrimers as Single-Photon Sources. *J. Phys.: Condens. Matter* **2007**, *19*, 445004.
51. Vosch, T.; Cotlet, M.; Hofkens, J.; Van der Biest, K.; Lor, M.; Weston, K. D.; Tinnefeld, P.; Sauer, M.; Latterini, L.; Müllen, K.; *et al.* Probing Förster Type Energy Pathways in a First Generation Rigid Dendrimer Bearing Two Perylene Imide Chromophores. *J. Phys. Chem. A* **2003**, *107*, 6920–6931.
52. Flors, C.; Oesterling, I.; Schnitzler, T.; Fron, E.; Schweitzer, G.; Sliwa, M.; Herrmann, A.; Van der Auweraer, M.; De Schryver, F. C.; Müllen, K.; *et al.* Energy and Electron Transfer in Ethynylene Bridged Perylene Diimide Multichromophores. *J. Phys. Chem. C* **2007**, *111*, 4861–4870.
53. Hofkens, J.; Maus, M.; Gensch, T.; Vosch, T.; Cotlet, M.; Köhn, F.; Herrmann, A.; Müllen, K.; De Schryver, F. C. Probing Photophysical Processes in Individual Multichromophoric Dendrimers by Single-Molecule Spectroscopy. *J. Am. Chem. Soc.* **2000**, *122*, 9278–9288.
54. Becker, K.; Gaefke, G.; Rolffs, J.; Höger, S.; Lupton, J. M. Quantitative Mass Determination of Conjugated Polymers for Single Molecule Conformation Analysis: Enhancing Rigidity with Macrocycles. *Chem. Commun.* **2010**, *46*, 4686–1688.
55. Mirzov, O.; Bloem, R.; Hania, P. R.; Thomsson, D.; Lin, H.; Scheblykin, I. G. Polarization Portraits of Single Multichromophoric Systems: Visualizing Conformation and Energy Transfer. *Small* **2009**, *5*, 1877–1888.
56. Camacho, R.; Thomsson, D.; Yadav, D.; Scheblykin, I. G. Quantitative Characterization of Light-Harvesting Efficiency in Single Molecules and Nanoparticles by 2D Polarization Microscopy: Experimental and Theoretical Challenges. *Chem. Phys.* **2012**, *406*, 30–40.
57. Trinkunas, G.; Herek, J. L.; Polívka, T.; Sundström, V.; Pullerits, T. Exciton Delocalization Probed by Excitation Annihilation in the Light-Harvesting Antenna LH2. *Phys. Rev. Lett.* **2001**, *86*, 4167–4170.
58. Weston, K. D.; Dyck, M.; Tinnefeld, P.; Müller, C.; Herten, D. P.; Sauer, M. Measuring the Number of Independent Emitters in Single-Molecule Fluorescence Images and Trajectories Using Coincident Photons. *Anal. Chem.* **2002**, *74*, 5342–5349.
59. Yang, J.; Park, M.; Yoon, Z. S.; Hori, T.; Peng, X.; Aratani, N.; Dedecker, P.; Hotta, J.-I.; Uji-I, H.; Sliwa, M.; *et al*. Excitation Energy Migration Processes in Cyclic Porphyrin Arrays Probed by Single Molecule Spectroscopy. *J. Am. Chem. Soc.* **2008**, *130*, 1879–1884.
60. Yoo, H.; Yang, J.; Nakamura, Y.; Aratani, N.; Osuka, A.; Kim, D. Fluorescence Dynamics of Directly Meso-Meso Linked Porphyrin Rings Probed by Single Molecule Spectroscopy. *J. Am. Chem. Soc.* **2009**, *131*, 1488–1494.
61. Masuo, S.; Vosch, T.; Cotlet, M.; Tinnefeld, P.; Habuchi, S.; Bell, T. D. M.; Oesterling, I.; Beljonne, D.; aChampagne, B.; Müllen, K.; *et al*. Multichromophoric Dendrimers as Single-Photon Sources: A Single-Molecule Study. *J. Phys. Chem. B* **2004**, *108*, 16686–16696.